Mechanism of Concentric Eyewall Replacement Cycles and Associated Intensity Change*

XIAQIONG ZHOU AND BIN WANG

International Pacific Research Center, and Department of Meteorology, School of Ocean and Earth Science and Technology, University of Hawaii at Manoa, Honolulu, Hawaii

ABSTRACT

To understand the mechanisms responsible for the secondary eyewall replacement cycles and associated intensity changes in intense tropical cyclones (TCs), two numerical experiments are conducted in this study with the Weather Research and Forecasting (WRF) model. In the experiments, identical initial conditions and model parameters are utilized except that the concentration of ice particles is enhanced in the sensitivity run. With enhanced ice concentrations, it is found that the secondary eyewall forms at an increased radius, the time required for eyewall replacement is extended, and the intensity fluctuation is relatively large. The enhanced concentrations of ice particles at the upper tropospheric outflow layer produces a noticeable subsidence region (moat) surrounding the primary eyewall. The presence of the moat forces the secondary eyewall to form at a relatively large radius. The axisymmetric equivalent potential temperature budget analysis reveals that the demise of the inner eyewall is primarily due to the interception of the boundary layer inflow supply of entropy by the outer convective ring, whereas the advection of low entropy air from the middle levels to the boundary inflow layers in the moat is not essential. The interception process becomes inefficient when the secondary eyewall is at a large radius; hence, the corresponding eyewall replacement is slow. After the demise of the inner eyewall, the outer eyewall has to maintain a warm core not only in the previous eye, but also in the moat. The presence of low equivalent potential temperature air in the moat results in the significant weakening of storm intensity. The results found here suggest that monitoring the features of the moat and the outer eyewall region can provide a clue for the prediction of TC intensity change associated with eyewall replacement.

1. Introduction

A full cycle of eyewall replacement includes the genesis of a secondary eyewall, the dissipation of the inner eyewall, and the organization of the new eyewall (Willoughby et al. 1982). Eyewall replacement is a very common phenomenon in intense tropical cyclones (TCs) (Hawkins et al. 2006; Kossin and Sitkowski 2009; Kuo et al. 2009). As the outer eyewall develops and migrates inward, the inner eyewall weakens and is eventually replaced by the outer one. The storm often weakens as a result of the gradual erosion of the inner eyewall, but it reintensifies when the outer eyewall contracts and gains organization. The prediction of intensity change associated with eyewall replacement cycles is still a challenge for forecasters because of lack of understanding of the complicated processes.

Previous studies have been focused on the genesis of secondary eyewalls. It is suggested that both internal and external dynamics could play important roles. Examples of internal dynamics are propagating vortex Rossby waves (VRWs) that interact with critical radius (Montgomery and Kallenbach 1997) and axisymmetrization of binary vortex interaction (Kuo et al. 2004, 2008). On the other hand, Nong and Emanuel (2003) suggested that finite-amplitude perturbations grow through the wind-induced surface heat exchange (WISHE) forming a secondary eyewall. They hypothesized that TC interaction with baroclinic eddies, topography, or sea surface temperature (SST) variations are likely to provide the typical perturbations needed for the formation.

Corresponding author address: Xiaqiong Zhou, University of Hawaii, 2525 Correa Rd., HIG 351A, Honolulu, HI 96822.
E-mail: xiaqiong@hawaii.edu

One debatable issue is whether the inclusion of ice is essential for the formation of secondary eyewalls. Based on the numerical results from an axisymmetric model, Willoughby et al. (1984) proposed that inclusion of ice in the model is a necessary ingredient. Their hypothesis further involves increasing convective instability at low levels and increasing upper-level inertial instability. Cooling from melting ice aloft invigorates the potential convective instability. To realize this potential convective instability, Willoughby et al. (1984) conjectured that the inertial instability of the upper-level outflow may create sufficient lift to overcome a low-level capping inversion. Nevertheless, observations (Molinari and Vollaro 1990) have revealed that inertial instability rarely occurs in the outflow layer. All TCs involve the ice phase, but not all storms produce concentric eyewalls. Terwey and Montgomery (2008) carried out two sensitivity experiments with and without ice particles. They found that the secondary eyewalls form in both experiments, and they suggest that ice microphysics is not a necessary ingredient for secondary eyewall formation. However, the secondary eyewall in no-ice experiment forms closer to the inner one and the inner eyewall collapses faster than in the ice experiment [see Figs. 3 and 11 in Terwey and Montgomery (2008)]. We speculated that the ice-phase microphysics may affect the behavior of eyewall replacement cycles although it is not essential for its formation.

Kossin and Sitkowski (2009) introduced an empirical model to provide forecasters with a tool to gauge the probability of imminent secondary eyewall formation based on the environmental variables and geostationary satellite features. The model performed skillfully enough against a defined climatology. However, observational studies reveal that the TC intensity changes associated with concentric eyewall replacement vary considerably from case to case. For example, an abrupt decrease in maximum wind speed (MWS) as large as 46 m s^{-1} was detected in Typhoon Sarah (1956), but the appearance of the concentric eyewalls in Hurricane Anita (1977) only marked the end of a deepening phase (Willoughby et al. 1982). Kuo et al. (2009) examined the intensity changes before and after concentric eyewall formation over the western North Pacific (WNP). About 28% of TCs actually intensify after the secondary eyewall formation. Moreover, by summarizing several cases of concentric eyewalls, Willoughby (1995) found that the time required for a cycle of weakening and reintensification can range from a few hours to more than a day. This implies that the prediction of intensity change associated with concentric eyewall cycles remains problematic even if we can predict its formation.

The aim of this study is to understand the variety of secondary eyewall replacement cycles and associated intensity changes. To fulfill this purpose, numerical sensitivity experiments with the Weather Research and Forecasting (WRF) model are conducted by changing ice-phase microphysics. The simulated eyewall replacement cycles are analyzed to reveal related physical processes. The model and experimental designs are described in section 2. The storm intensity and structure changes in the two experiments are compared in section 3. In section 4, the possible mechanisms responsible for different behaviors of eyewall replacement cycles are explored. A summary and discussion are presented in the last section.

2. Model and experimental design

The WRF model uses fully compressible, Eulerian nonhydrostatic equations with a mass vertical coordinate. The horizontal grid distributions follow the Arakawa C-grid staggering scheme. The model is conducted in a quadruply nested two-way interactive mode with the horizontal resolutions of 54, 18, 6, and 2 km, respectively and 28 levels in the vertical. The Kain–Fritsch convective scheme (Kain and Fritsch 1990, 1993) is applied in the two coarse meshes. An explicit cloud scheme (Lin et al. 1983) is used in the two fine meshes. In the Lin scheme, ice particles are grouped into three main classes: ice crystals, snow, and graupel. The Yonsei University (YSU) scheme (Noh et al. 2003) is chosen for the planetary boundary layer parameterization. The longwave and shortwave radiation is calculated with the Rapid Radiation Transfer Model (RRTM).

The model is initialized with an axisymmetric cyclonic vortex on an f plane centered at 18°N in a quiescent environment over the ocean with a constant sea surface temperature of 29°C. The initial vortex has a maximum surface wind speed of 15 m s^{-1} at a radius of 150 km, and the wind speed decreases with height. The mass and thermodynamic fields are obtained by solving a nonlinear balance equation for the given tangential wind fields. All the parameter settings for the initial vortex are identical to that described in Ge et al. (2008).

A sensitivity experiment (named ICE) is designed to investigate the impacts of ice-phase microphysics on concentric eyewalls replacement cycles. It makes use of the same initial conditions, model physics, and grid configuration as in the control run (CTL), except that the graupel sublimation in the cloud microphysics package is reduced by 50%. The range of graupel sublimation used here ensures that the response of ice concentrations to the modified microphysical process is well within
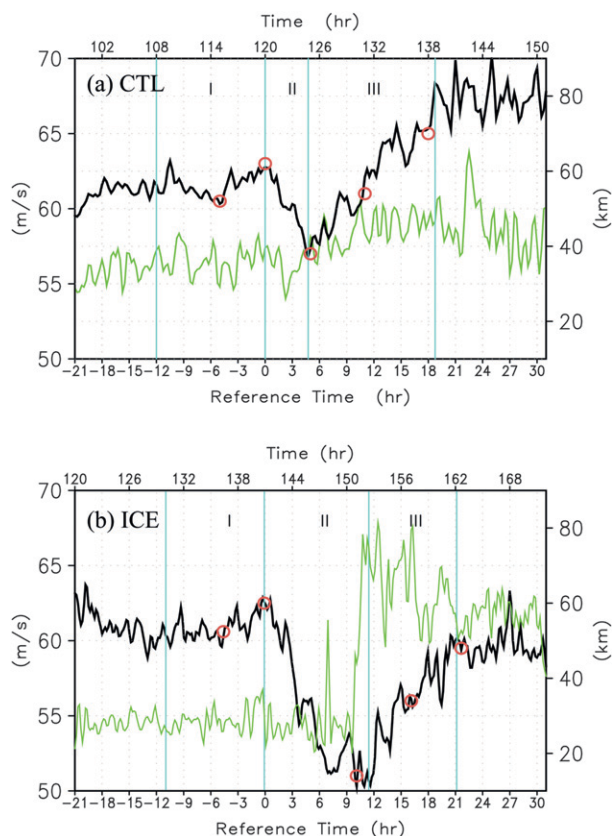
FIG. 1. Time series of storm intensity in the (a) CTL and (b) ICE experiments. The black curve represents the surface MWS and the green denotes RMW. The open circles correspond to the characteristic times used in Figs. 5–7. The time of model integration and the reference time with respect to the secondary eyewall formation are indicated at the upper and lower x axes. Three distinct phases—the formation of a secondary eyewall (I), the eyewall replacement (II), and the eventual formation of an annular hurricane (III)—are marked.

TABLE 1. Summary of eyewall replacement characteristics in the CTL and ICE experiments.

	CTL	ICE
Formation of secondary eyewall		
Model time (h)	120	141
Radial location (km)	70–90	100–120
Strength	Stronger	Weaker
Intensity change (Vmax)		
Initial weakening	-5 m s^{-1} in 5 h	-12 m s^{-1} in 11 h
Reintensification	$+10$ m s^{-1} in 14 h	$+8$ m s^{-1} in 10 h
Time for the demise of inner eyewall or eyewall replacement	Faster (9 h)	Slower (21 h)
Formation of an annular hurricane		
RMW (km)	40	55
Intensity	Stronger after replacement	Slightly weaker after replacement

MWS of about 60 m s^{-1}. It is close to the average intensity of the observed TCs with concentric eyewall structure (Hawkins et al. 2006; Kossin and Sitkowski 2009). The secondary eyewall in CTL emerges at about 120 h, which is almost one day early than that in the ICE (Fig. 1). It seems that the increased ice concentrations tend to delay the formation of the secondary eyewall.

For convenience, a new time coordinate corresponding to our focused interest is defined thereafter. The time of the secondary eyewall formation in the simulation is labeled 0 h in the new time coordinate. Table 1 presents a summary of the contrasting structure and intensity changes during the concentric eyewall replacement processes between CTL and ICE.

Figure 1 illustrates the evolution of the MWS near the surface and the radius of maximum wind (RMW) during the eyewall replacement. In CTL, the MWS drops by about 5 m s^{-1}, followed by a salient reintensification with an increase of the MWS by about 10 m s^{-1} (Fig. 1a). The reintensification overwhelms the weakening so that the storm in CTL exceeds its original intensity after eyewall replacement. In ICE, the storm intensity decreases by 12 m s^{-1} within 11 h followed by a recovery in the MWS. The storm is slightly weaker after the replacement. In general, the intensity fluctuation is more significant in ICE than in CTL.

The RMW in ICE leaps from 30 to 70 km as a result of the marked weakening of the inner eyewall and the strengthening of the outer one (Fig. 1b). Thereafter, it gradually contracts to 55 km. In sharp contrast, there is no abrupt change of the RMW in CTL. The RMW increases from 35 to 45 km and then contracts slightly, reaching a steady state at a radius of 40 km (Table 1).

realistic limits given the observational uncertainties of the cloud processes but also yields significant changes in the behaviors of the secondary eyewall replacement. More importantly, the modification does not change storm steady-state intensity significantly. The model was integrated for 9 days with outputs every 10 min during the period of interest. The concentric eyewall replacement cycle in CTL has been discussed by Zhou and Wang (2009). In this study, we mainly focus on the differences existing between CTL and ICE.

3. Eyewall replacement cycles

a. Intensity and structural change

The storms in the two experiments spin up rapidly and reach a relatively steady state after 48 h with a surface
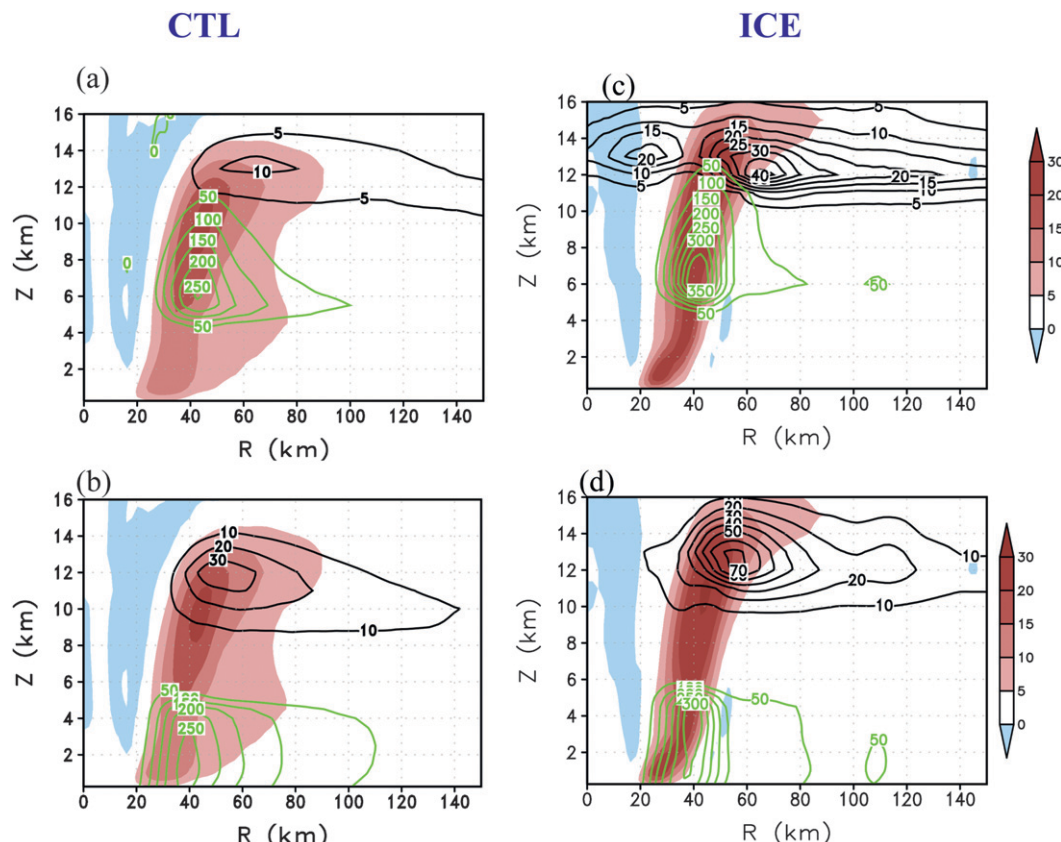
FIG. 2. Radius–height distributions of the concentrations of (a) graupel (green contours) and cloud ice (black contours) and (b) rainwater (green contours) and snow (black contours) averaged during the period from −21 to −11 h in CTL (10^{-2} g kg^{-1}). (c),(d) As in (a),(b), but for the ICE experiment. The shading is the axisymmetric vertical motion (cm s^{-1}).

b. The time-mean symmetric structures prior to the secondary eyewall formation

Figures 2 and 3 compare the time-mean symmetric structures prior to the second eyewall formation. The storms in both CTL and ICE have an outward-sloping eyewall and subsidence in the eye as shown in the vertical motion fields (Figs. 2a,b). High concentrations of graupel are found mainly in the strong updrafts in the eyewalls (Figs. 2a,c). The maximum is located at the height of 6 km, below which is a sharp decline, reflecting the melting of graupel at the 0°C level. Snow and cloud ice are found primarily in the upper troposphere in strong updrafts and just radially outward, where the frozen condensate is advected by the outflow stream. The maximum center is located at a height of 12 km near the −40°C isotherm (not shown). It partly reflects the freezing by homogeneous nucleation, where all cloud water converts spontaneously to cloud ice (Lin et al. 1983).

Nevertheless, in CTL the eyewall is weaker and much broader than in ICE. There is an area of mesoscale ascent extending 20–40 km out in the eyewall. The reduction of

graupel sublimation increases the graupel amount by about 40%. The modification of the microphysics scheme also results in strengthened updrafts in the eyewall and remarkably enhanced snow and ice concentrations.

The maximum axisymmetric tangential wind center is located just near the top of the boundary layer, at the height of 1.5 km in the eyewall in both experiments (Fig. 3). The storm intensity is slightly weaker, but its size is larger in CTL than in ICE prior to the secondary eyewall formation. Figures 3a and 3d show that the maximum symmetric wind speed is 79 m s^{-1} in CTL and 82 m s^{-1} in ICE. Strong winds extend to a larger radius at the low levels in CTL than in ICE. Radial inflow layer is up to 5 km high in CTL at the outer region, while it is mainly confined to a shallow layer 1–2 km above the surface in ICE. This result is consistent with Lord et al. (1984)'s work where an axisymmetric model is employed. The deeper inflow layer is likely a response to the more active convection in the outer region in CTL (Shapiro and Willoughby 1982).

The microphysics process modification also considerably alters the diabatic heating profiles (Figs. 3c,f). Ice
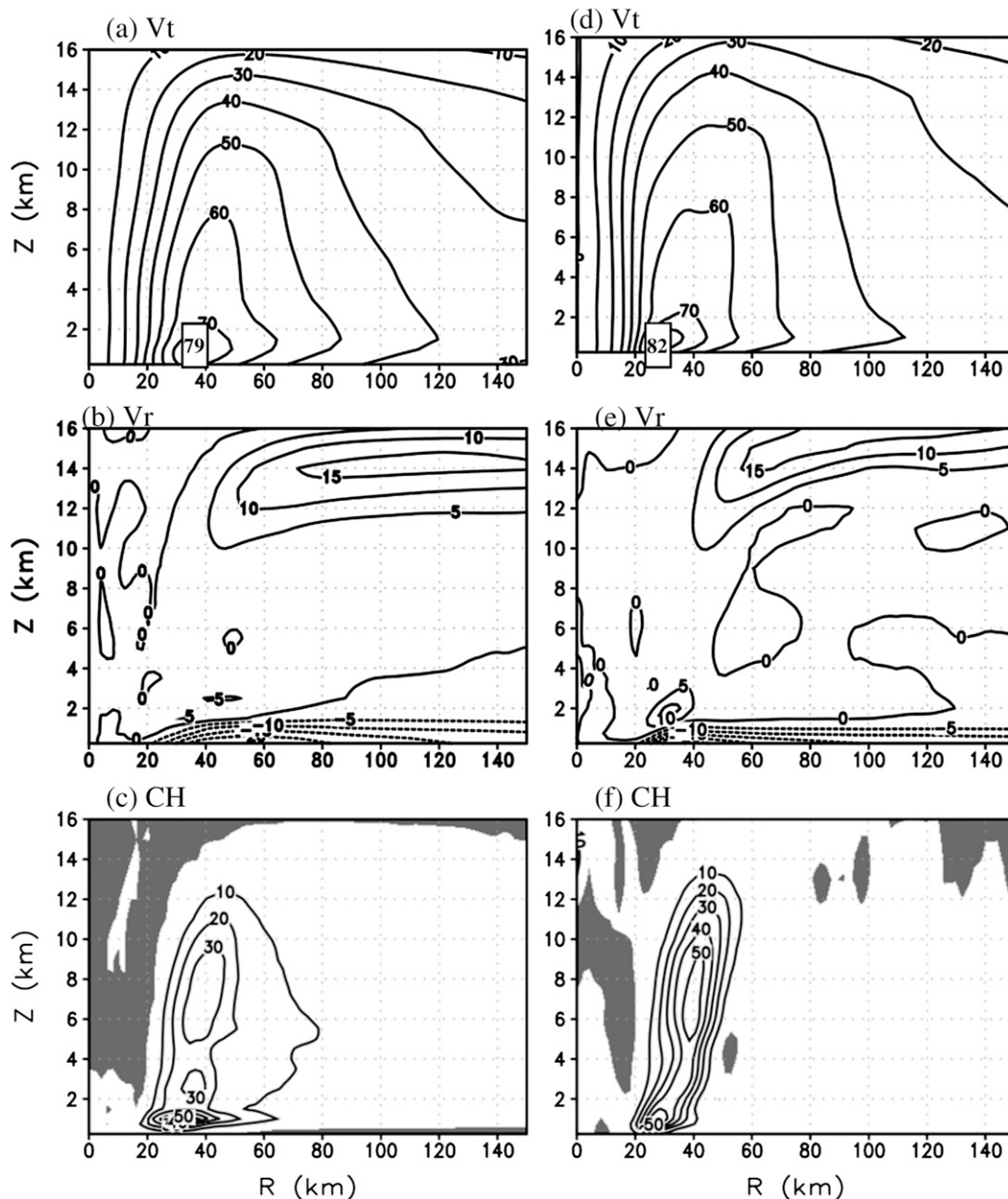
FIG. 3. Radial–vertical structures of axisymmetric (a) tangential winds, (b) radial winds, and (c) condensation heating (K h^{-1}) averaged during the period from −21 to −11 h for CTL. (d)–(f) As in (a)–(c), but for ICE. Diabatic cooling is shaded in (c) and (f).

precipitation in ICE is enhanced, so the upper-level maximum heating, which corresponds to cold rain processes, is much stronger than in CTL. The latent heat release at low levels related to warm rain processes dominates in CTL.

c. Eyewall replacement cycles

In this section, the eyewall replacement cycles are compared in three distinct phases: the formation of a secondary eyewall, the eyewall replacement, and the organization of the new eyewall.

Figure 4 compares the evolution of the axisymmetric midlevel vertical motion and tangential velocity at the 3-km level. In phase I, the storm intensity remains almost constant in CTL and ICE (Fig. 1). In ICE, convection emerges at a radius greater than 80 km away from the TC center as evidenced by the upward motion; between the eyewall and the outer rainbands is a wide region of
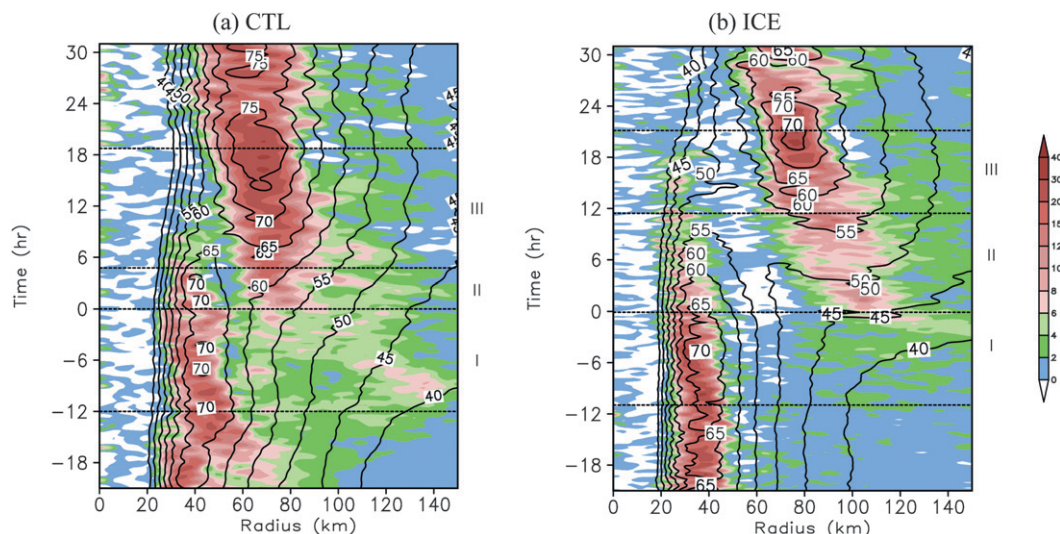
FIG. 4. Radius–time Hovmöller diagrams of the azimuthal mean vertical velocity at the height of 5 km (shading, cm s^{-1}) and tangential velocity at 3-km height (contour, m s^{-1}) for (a) CTL and (b) ICE.

weak subsidence (from 50 to 80 km), usually referred to as the moat, whereas there is no clear moat in CTL. Meanwhile the convection outside the primary eyewall is more active in CTL than in ICE. In phase II, the storm intensity starts to weaken (Fig. 1). In ICE, two deep convective rings are located at 20–40 km and 100–120 km, and the separation distance between them reaches 60 km. The appearance of the second convective maximum apparently enhances the descending motion in the moat. In CTL, however, the two concentric eyewalls are located at 30–50 km and 70–90 km. They are much closer to each other in CTL than in ICE. In phase III, the new convective ring dominates, and the storm reintensifies significantly

with the contraction and strengthening of the new eyewall. Note that the inner eyewall lasts about 9 h in CTL after the secondary eyewall formation, much shorter than in ICE (~21 h).

The storm horizontal structures at the different stages are compared in Fig. 5. In general, the storms experience similar structural evolution in these two experiments. The original eyewalls are an annulus of high rainwater concentration. The outer rainbands remain active and eventually form their own convective ring. Two convective rings are concentric to the storm center. Thereafter, the inner ring fades away, and the outer ring supplants the original one, forming a storm with typical
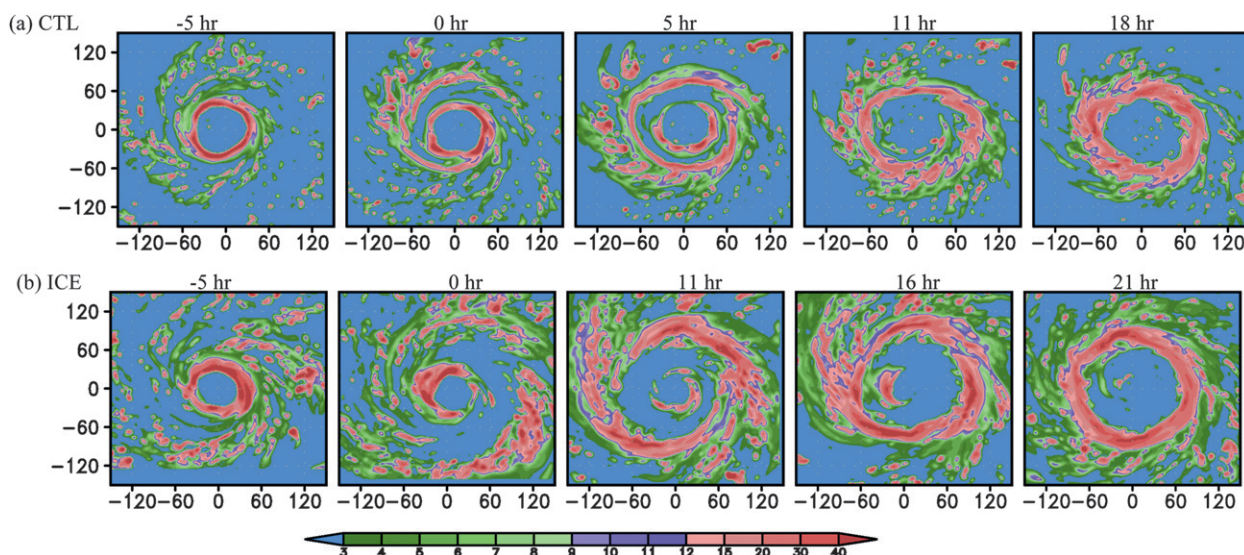

FIG. 5. Rainwater distributions (0.1 g kg^{-1}) at 550 hPa in the (a) CTL and (b) ICE experiments.
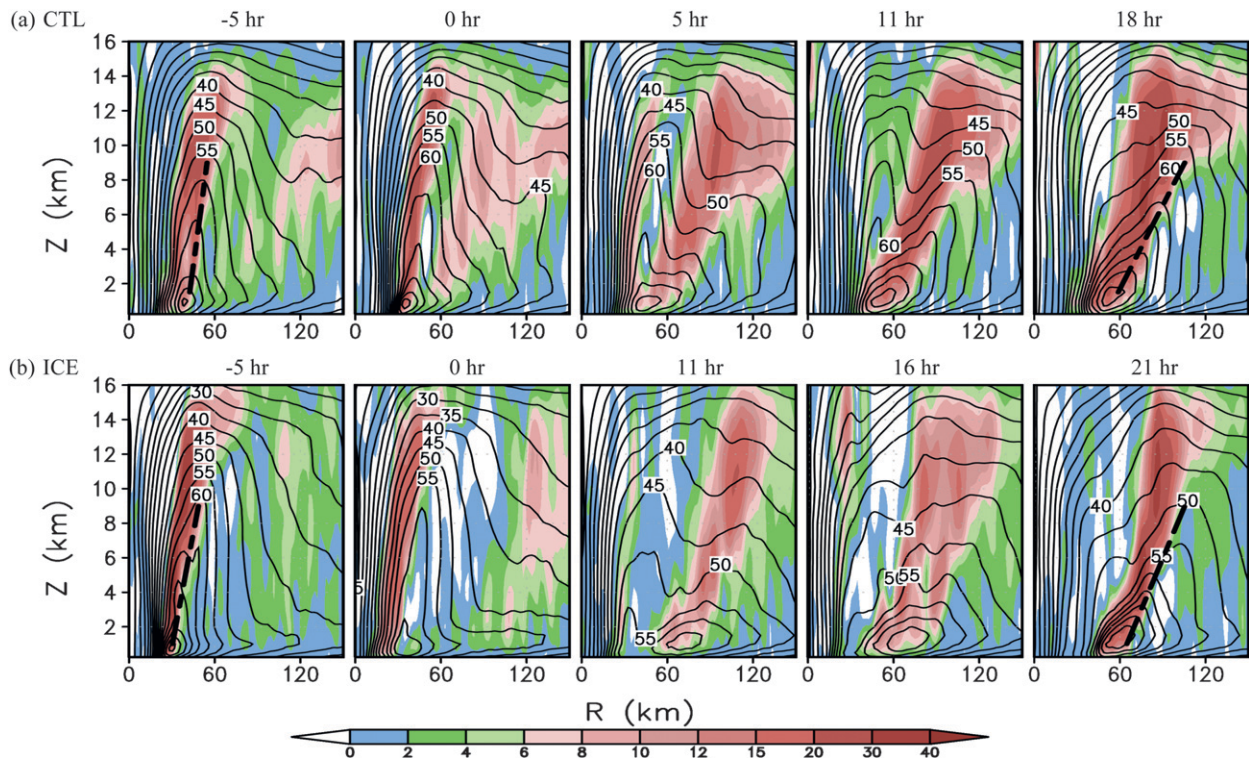
FIG. 6. Radius–vertical distributions of azimuthal mean vertical velocity (shading, cm s^{-1}) and tangential winds (contour, m s^{-1}) in (a) CTL and (b) ICE. Dashed lines mark the RMW for the original eyewall and the new eyewall after eyewall replacement.

features of an annular hurricane (AH): a large eye, a broad eyewall, and quasi-axisymmetric structures (Knaff et al. 2003, 2008). The new storm in ICE has a relatively larger eye than in CTL, since the outer eyewall forms at a larger radius.

Figure 6 compares the radial–vertical cross section of the azimuthal mean tangential wind and vertical velocity. The secondary wind maxima are generally collocated with the convective ring, analogous to the collocation of the peak winds and the convection in the inner eyewall. Consistent with observations (Houze et al. 2007), the outer eyewalls have a larger outward vertical tilt than the inner ones. As a result, the width of the moat increases with height. The concentric eyewalls almost merge together near the surface in ICE.

Figure 7 further compares the tangential wind profiles in CTL and ICE. Prior to the formation of the secondary eyewall at −5 h, the radial wind profile at 700 hPa is broader in CTL. With the development of a secondary eyewall, the outer tangential winds in both experiments increase noticeably. A secondary tangential wind maximum is apparent in ICE as a secondary eyewall forms at 0 h, but it is absent in CTL until 5 h. The absence of two wind peaks is ascribed to the sufficient mixing between two concentric eyewalls. Further discussion can be found

in the following section. The secondary wind maximum exceeds the inner one at the end of the replacement. The storms have a much broader wind profile and the RMW becomes larger after the eyewall replacement in these two experiments.

Overall, the simulated concentric eyewall replacement cycles in both CTL and ICE are consistent with the conventional concepts (Willoughby et al. 1982). The outer eyewall presents a larger outward tilt in the vertical as observed by Houze et al. (2007). The storms experience intensity fluctuations during eyewall replacement. In addition, after the eyewall replacement, the storms in both CTL and ICE turn into an annular hurricane. It confirms that the concentric eyewall replacement is a route to the formation of an AH (Zhou and Wang 2009).

Nevertheless, the simulated eyewall replacement cycles exhibit significant differences (Table 1), including the location of the secondary eyewall formation, the time of eyewall replacement, and the amplitude of intensity fluctuation. With enhanced concentrations of ice particles, the secondary eyewall forms at a larger radius, and thus a moat can be easily identified. Meanwhile, the time for the eyewall replacement is longer, and the storm experiences larger intensity fluctuation. The results
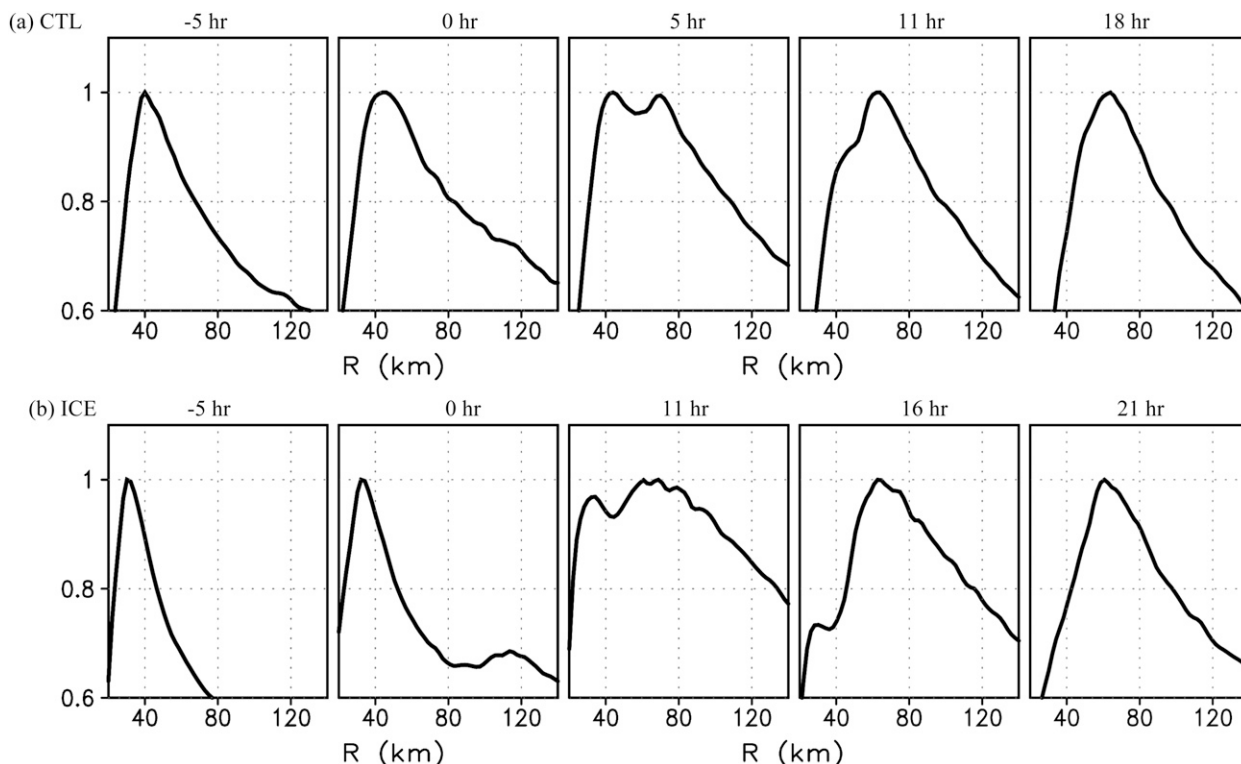
FIG. 7. Tangential wind profiles at 700 hPa normalized by the maximum wind simulated in (a) CTL and (b) ICE.

suggest that ice-phase microphysics indeed play an important role in modifying concentric eyewall replacement cycles.

4. The mechanisms of the eyewall replacement cycle

To understand the different behaviors simulated in these two experiments, we performed diagnostic analyses on four main aspects of secondary eyewall replacement cycles: the genesis of a secondary eyewall, the dissipation of the inner eyewall, the associated intensity change, and the subsequent formation of an AH.

a. What affects the radial location of secondary eyewall formation?

A good explanation of the physical processes responsible for the secondary eyewall formation has not been established so far. Some previous studies suggested the location of the secondary eyewall is likely determined by TC dynamical structures. Since the formation of a secondary eyewall is concurrent with the formation of a moat, the radial location of the secondary eyewall is also determined by the width of the moat. Rozoff et al. (2006) proposed that the moat might not be dominated only by subsidence. It is dynamically unfavorable for

deep moist convection. A strong filamentation process related to the swirl tangential flows tends to shear apart nascent convective cells before they can mature and organize. Cumulonimbus convection is potentially suppressed in the regions where the filamentation time is less than 30 min, a characteristic value for deep moist convective overturning. It is suggested that the secondary eyewalls only form in the region with moderate filamentation where convection is allowed to grow before straining processes disrupt deep convective updrafts.

Figures 8a and 8d show that the mean filamentation time scale associated with the straining portion of the flow increases with the radius. The region with a filamentation time greater than 30 min stretches from about 70 km outward in both CTL and ICE. According to the filamentation dynamics, secondary eyewalls only form outside of 70 km.

In addition to the moderate filamentation, Terwey and Montgomery (2008) proposed that a region with a weak negative radial potential vorticity (PV) gradient associated with the primary swirling flow (the β skirt) is required for secondary eyewall formation. Deep convection within the β skirt acts as a source of perturbation eddy kinetic energy and vorticity. A finite-amplitude, lower-tropospheric cyclonic jet outside the primary eyewall with a jet width on the order of a local effective β
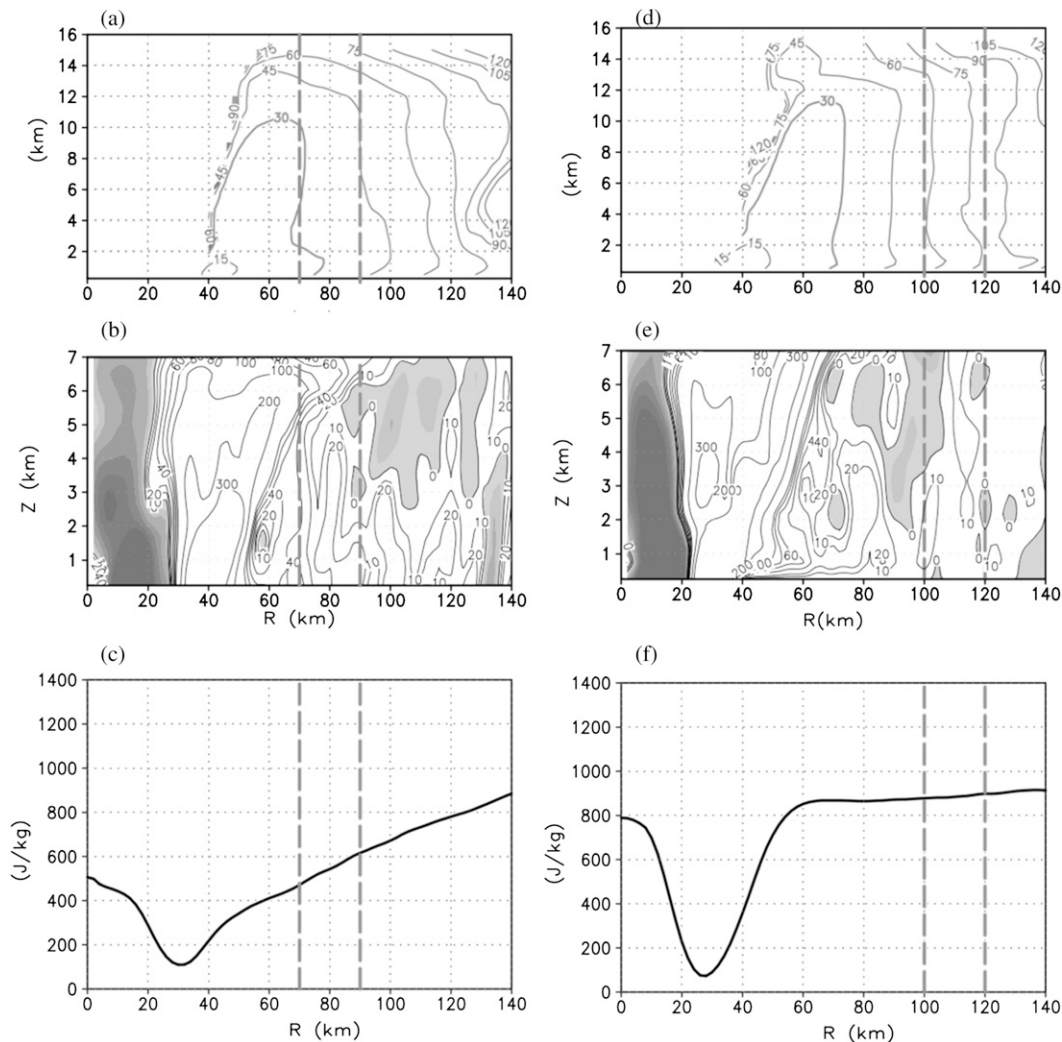
FIG. 8. (a) Time scales (min) associated with the straining portion of the flow, (b) β skirt (10^{-9} m^2 s^{-2}; negative β regions are shaded), and (c) CAPE (J kg^{-1}) averaged from -21 to -11 h in CTL. (d)–(f) As in (a)–(c), but for ICE. Two dashed lines roughly mark the radial location of the secondary eyewalls at 0 h.

scale might be generated by the axisymmetrization of convectively generated vorticity anomalies in this region. Thereafter, secondary eyewalls forms through the WISHE mechanism (Emanuel 1986).

The effective β is calculated following Terwey and Montgomery (2008)'s formula:

$$\beta = -\left(\frac{\partial \langle q \rangle}{\partial r}\right) \times \frac{\langle \xi \rangle}{\langle q \rangle},$$

where q is the Ertel PV, $\xi = f_0 + 2v_t$ is the modified Coriolis parameter, v_t is the mean tangential velocity and $\langle F \rangle$ indicates a temporal and azimuthal average of the quantity F. The positive sign of β means a decrease in PV with increasing radius. As shown in Figs. 8b and

8e, β changes sign at the middle troposphere, while the β skirt is identified in the lower troposphere beyond 40 km in CTL and between 40 and 120 km in ICE.

In the context of the β skirt and the filamentation time scale, a secondary eyewall could possibly form in the region between 70 and 120 km in both CTL and ICE. As marked in Fig. 8, the real location is at a radius of 70–90 km in CTL and 100–120 km in ICE, which is within the estimated range (70–120 km). It indicates that the above dynamical factors may play a role in determining the location of a secondary eyewall. However, this rough estimation apparently cannot elucidate the difference that exists between CTL and ICE.

Another dynamical process involves VRWs (Montgomery and Kallenbach 1997). It is suggested

that VRWs can accelerate the mean tangential flow at some distance from the storm center through eddy momentum flux convergence. This process could trigger a secondary wind maximum, a necessary condition for the secondary eyewall formation (Samsury and Zipser 1995). Our results resemble Judt and Chen (2010)'s simulation of Hurricane Rita (2005). There is no outward propagation of VRW-like eddies (not shown). The asymmetric eddies in the primary eyewall and in the outer region are separated with the moat. Whether VRWs play an essential role in the formation of a secondary eyewall in a realistic storm deserves further study.

It is also suggested that sufficient convective available potential energy (CAPE) is required for the formation of a secondary eyewall (Terwey and Montgomery 2008). Figure 8c shows that the CAPE in CTL increases gradually with radius, reaching 900 J kg^{-1} at 140 km. For the storm in ICE, CAPE increases to 1000 J kg^{-1} rapidly outside the primary eyewall and then decreases slightly farther outward (Fig. 8e). It is not clear how much CAPE is sufficient for convection occurrences. The secondary eyewall seems to form in the region with relatively low CAPE in CTL. To some degree, CAPE reflects convective activities. Low CAPE appears in the region with active convection due to sufficient consumption of moist convective instability. It remains unclear whether the distribution of CAPE in the outer region affects the radial location of secondary eyewalls.

Snow was deemed important for initiation and maintenance of broad-scale downdrafts, considered indicative of stratiform rain by Lord et al. (1984). Cooling due to melting of snow particles as they fall into warm air maintains downdrafts. Lord et al. (1984) found that the horizontal scale of the moat in TCs depends critically on both the horizontal advection of the snow particles detrained from the tops of convective updrafts and the mean falling speed of the particles toward the melting levels. The ICE experiment shows that cloud ice and snow spread outward from the primary eyewall in the upper troposphere. The relatively heavy concentrations of rainwater at lower levels occur at the same coordinates, corresponding to the fallout pattern of snow and rain (Fig. 2). Higher concentrations in snow likely contribute to a widespread subsidence region surrounding the primary eyewall in ICE. The presence of the wide moat determines that deep moist convection, as well as the secondary eyewall, occurs at the large radius.

b. Causes of the demise of inner eyewalls

After the formation of the secondary eyewall, the inner eyewall progressively dissipates. The dissipation of the inner eyewall is found to be more abrupt in CTL

than in ICE (Fig. 4). As suggested by Willoughby et al. (1982), the inner eyewall collapses as a direct result of subsidence induced diabatically by the outer eyewall. When the two eyewalls are close to each other, the inner one might be readily affected by the secondary eyewall. Nevertheless, the analytical solutions derived by Rozoff et al. (2008) do not support this hypothesis. They examined the effect of the diabatic heating in the outer eyewalls by using the transverse circulation equation associated with a balanced vortex model. Using a parameterization that distinguishes five radial regions, they found that the subsidence induced by the outer eyewall is primarily within the eye and the moat. In the present study, we found that the formation of the secondary eyewall enhanced the subsidence in the moat (Fig. 4), but it is difficult to identify whether the weakening of the inner eyewall results from the subsidence directly induced by the outer eyewall.

Other studies proposed that the outer eyewall may create hostile conditions for the inner eyewall through direct or indirect boundary layer interactions. In the direct mechanism, the outer eyewall cuts off the boundary layer inflow to the inner eyewall and the inward radial flux of moist entropy (Willoughby et al. 1982; Samsury and Zipser 1995; Rozoff et al. 2008). The indirect mechanism emphasizes the critical role of the downdrafts in the moat induced by latent heating released in secondary eyewalls. The downdrafts would transport low-entropy air from the middle level to boundary layer inflow, which chokes off convection and high vorticity in the inner eyewall (Shapiro and Willoughby 1982; Barnes et al. 1983). The inner eyewall might readily dissipate in ICE, since the subsidence surrounding the inner eyewall is stronger, but this is not the case.

To qualitatively estimate the direct and indirect effects, we performed an axisymmetric equivalent potential temperature θ_e budget analysis (see appendix). The contributions of updrafts and downdrafts (VADV1 and VADV2), the mean horizontal advection (MHADV), and horizontal eddy (HEDDY) to the azimuthal mean θ_e tendency after the formation of the secondary eyewall are calculated (Figs. 9 and 10). Strong inward cold advection in the boundary layer is confined to the boundary layer close to the eyewalls, primarily offset by the horizontal eddies and the vertical mixing, including the enthalpy flux from the ocean surface. The asymmetric eddies tend to mix large θ_e outward from the eyewalls. Negative tendency associated with the downdrafts is distinct between the concentric eyewalls. It covers a larger area and extends downward to the lower levels in ICE than in CTL. The contribution of updrafts is slightly weaker in ICE than in CTL but remains large enough to offset the contribution of downdrafts. This indicates that
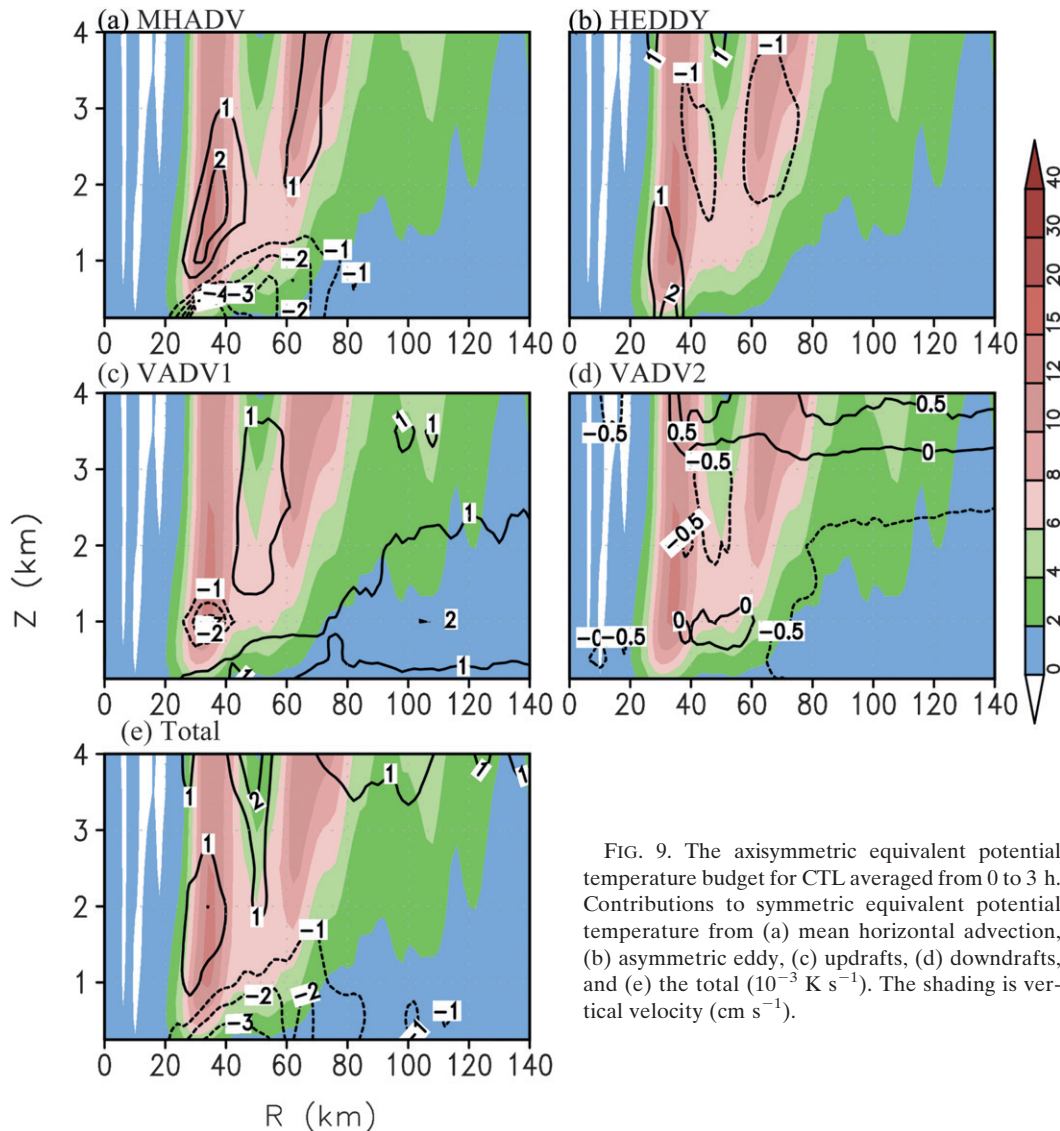
FIG. 9. The axisymmetric equivalent potential temperature budget for CTL averaged from 0 to 3 h. Contributions to symmetric equivalent potential temperature from (a) mean horizontal advection, (b) asymmetric eddy, (c) updrafts, (d) downdrafts, and (e) the total (10^{-3} K s^{-1}). The shading is vertical velocity (cm s^{-1}).

the indirect mechanism is not essential to the collapse of the inner eyewall.

The direct interception effect can be estimated from the horizontal advection of θ_e below the inner eyewall in the boundary layer. There is a much larger cold θ_e advection to the inner eyewall at the boundary layer in ICE than in CTL. The inner eyewall dissipates abruptly in CTL because of the difficulty of maintaining a high-entropy air column.

The horizontal advection, determined by azimuthal mean boundary inflow and the radial gradient of θ_e, is stronger in CTL than in ICE. The secondary eyewall, acting as a heating source in the outer region, induces a local convergent boundary layer flow, which offsets the boundary layer inflow toward the inner eyewall. The inflow cutoff is therefore more efficient in CTL because

the secondary eyewall is closer to the inner eyewall. In addition, the radial gradient of θ_e outside of the inner eyewall is larger in CTL than in ICE (Fig. 11). The θ_e fields in a TC usually have an in–up–out pattern and change markedly as one proceeds inward to the center. Isotherms of θ_e concentrate in the eyewalls, rise nearly vertically, and decrease rapidly with the radius. The radial gradient of θ_e is large outside the inner eyewall in CTL when the outer eyewall is close to the inner one. Conversely, as the secondary eyewall forms at a larger radius in ICE, the vertically oriented θ_e in the secondary eyewall has a relatively smaller effect on the inner one. The boundary layer θ_e remains almost constant before flowing into the inner eyewall. The inner eyewall vanishes only when the secondary eyewall contracts and increases
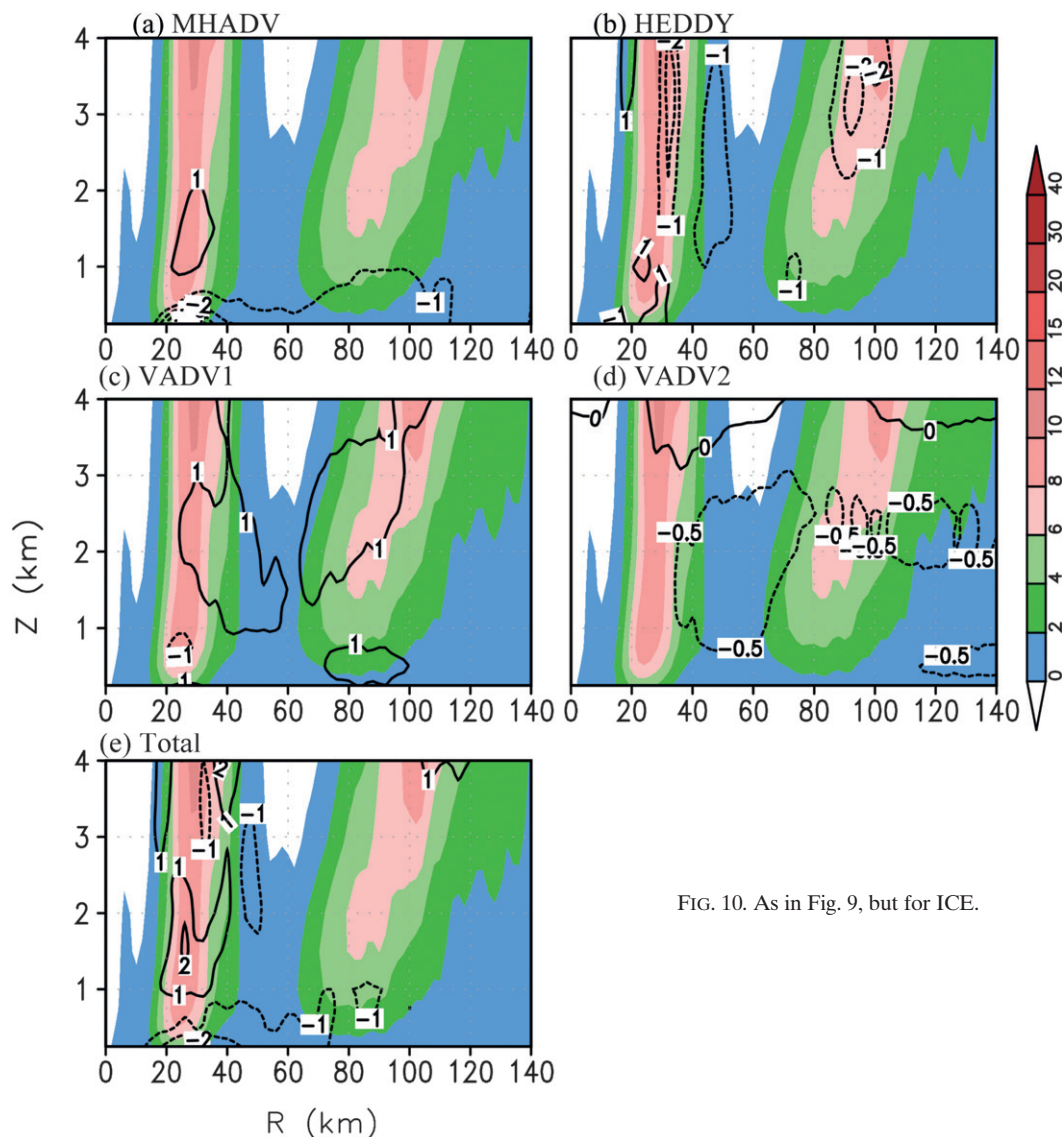
FIG. 10. As in Fig. 9, but for ICE.

the radial θ_e gradient outside of the inner eyewall. The results here suggest that the direct effect of the outer eyewall is related to the separation displacement between two concentric eyewalls. The secondary eyewall, forming at a larger (smaller) radius, takes a longer (shorter) time period to replace the inner eyewall.

The dependence of the time period of eyewall replacement on the location of the secondary eyewall is further examined by conducting a series of sensitivity experiences. A nudging technique is applied to force a secondary eyewall to form at different radii (Liu et al. 2005). Prior to the secondary eyewall formation (i.e., at 96 h), the low-level wind field is forced for 12 h with wind anomaly 10 m s^{-1} at radii of 80 and 100 km. It is applied only to the low-level winds, since the low-level jet is considered essential to induce secondary eyewall

formation through the WISHE mechanism (Nong and Emanuel 2003; Terwey and Montgomery 2008). The inner eyewall, especially in the experiment with the forcing at the radius of 80 km, weakens significantly during the nudging period. The outer eyewall is successfully forced to form at radii of 60–80 and 80–100 km. Note that there is a significant contraction of the outer eyewall after the nudging is turned off. We continue to run the model until the eyewall replacement cycle is complete. Figure 12 shows that the inner eyewall is taken over in 6 ($>$12) h in the experiment with the wind nudging at the small (large) radius (Fig. 12).

c. Intensity change

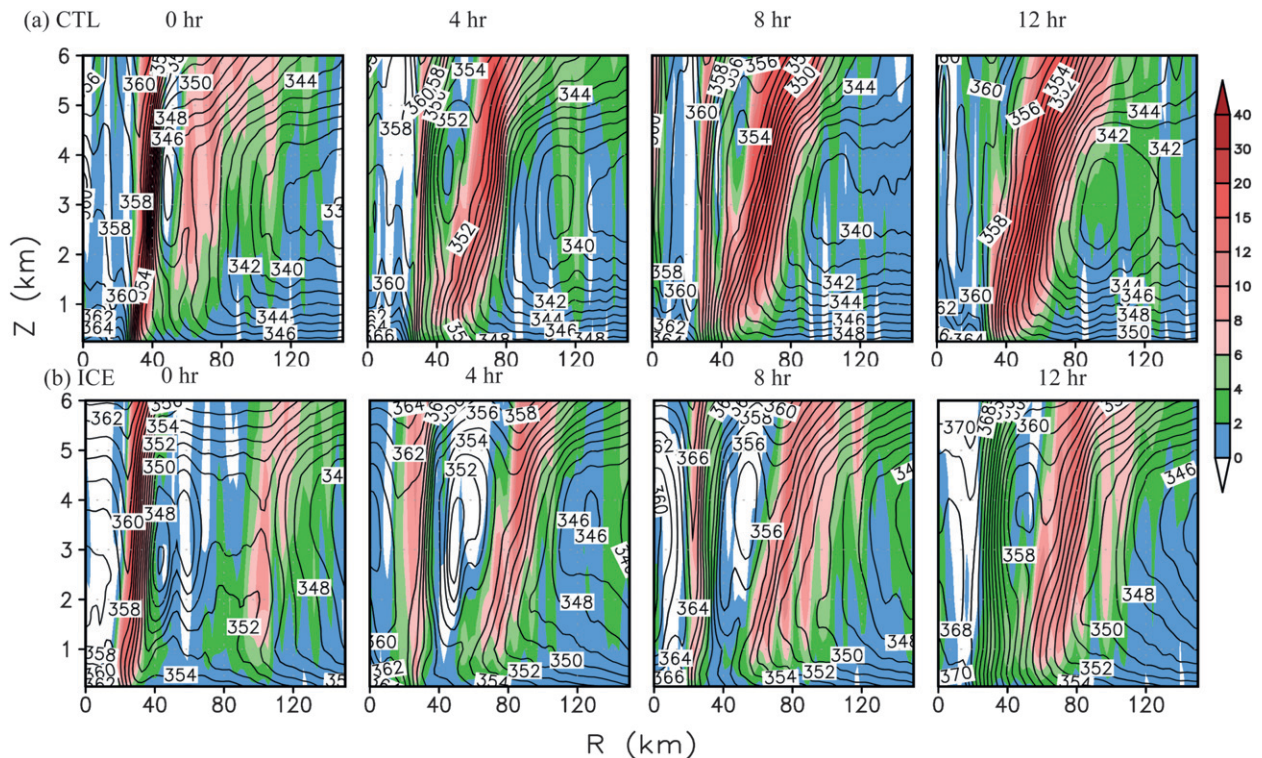The weakening of storm intensity usually coincides well with the demise of the inner eyewall. As the inner

FIG. 11. The evolution of axisymmetric equivalent potential temperature (contour) after the formation of the secondary eyewall in (a) CTL and (b) ICE. The shading is vertical velocity (cm s^{-1}).

eyewall dies, the storm temporarily loses its ability to produce an intense, localized warm core (Rozoff et al. 2008). Moreover, the moat with relatively low θ_e becomes a part of the eye after the inner eyewall fades away. Apparently, the air in the moat is much cooler than that in the eye. The new eyewall must have the ability to maintain a warm core not only in the previous eye but also in the moat region in order to prevent the
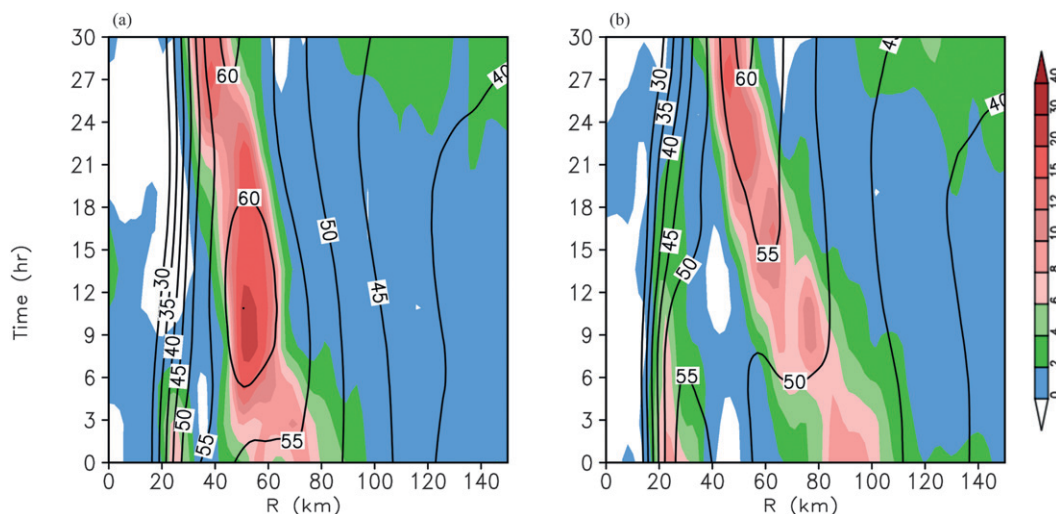

FIG. 12. Radius–time Hovmöller diagrams of the azimuthal mean vertical velocity at 5-km height (shading, cm s^{-1}) and tangential velocity at 3-km height (contour, m s^{-1}) for the experiments with the tangential wind nudging at (a) 80 and (b) 100 km. Hour 0 is the time when the nudging stops.
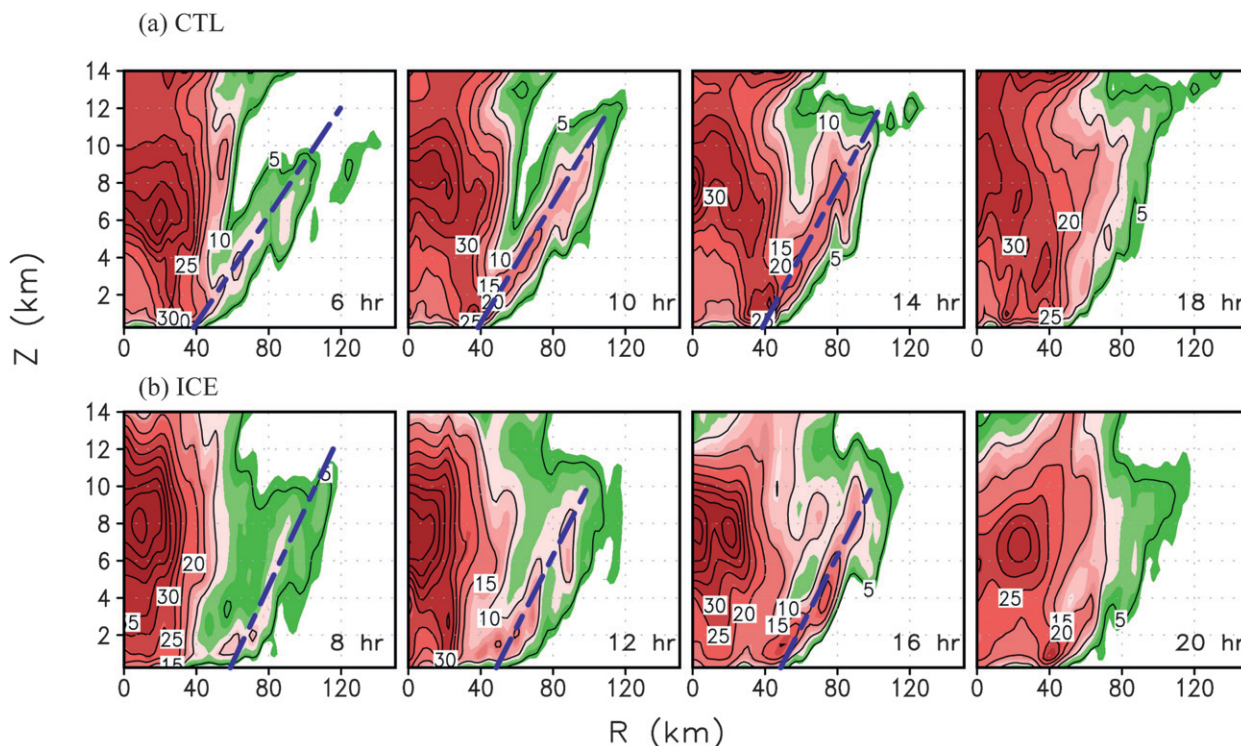
(a) CTL

(b) ICE

FIG. 13. Simulated radius–vertical distributions of axisymmetric potential vorticity [0.1 potential vorticity unit (PVU)] during and after the eyewall replacement in (a) CTL and (b) ICE. Dashed lines mark the enhanced PV in the secondary eyewalls.

weakening of storm intensity. To recover its intensity, the filling of low θ_e in the moat is required. The width and thermodynamic features of the moat could markedly affect the intensity change during eyewall replacement. The θ_e fields indicate a persistent center of low θ_e at the height of 3 km between the eyewalls (Fig. 11). Given that the moat in CTL is much narrower and weaker than in ICE, the low θ_e there is filled more rapidly in CTL (8 h) than in ICE (about 16 h). As a result, the weakening of the storm intensity is more remarkable in ICE than in CTL.

d. Formation of an annular hurricane

The concentric eyewall replacement cycles in both CTL and ICE lead to the formation of an AH with a broad eyewall and a large eye. As suggested by Zhou and Wang (2009), the sufficient mixing of enhanced PV in concentric eyewalls plays an important role in the formation of an AH. Two convective rings are associated with enhanced PV. The radial gradient of vorticity changes signs twice from the inner eyewall to the outer eyewall. If the moat between these two eyewalls is sufficiently narrow, barotropic instability may occur (referred to as type II instability by Kossin et al. 2000). Figure 13 exhibits the radial–vertical distribution of PV during and after the eyewall replacement. As shown in

CTL, the enhanced PV corresponding to the inner and outer eyewalls is mixed gradually from low levels to upper levels since the width of the moat increases with height. Sufficient mixing between the concentric eyewalls is also responsible for the absence of two wind peaks when the secondary eyewall forms in CTL (Fig. 7). During the PV mixing period, the eyewalls are usually elliptical in shape (not shown), which indicates the presence of wavenumber-2 instability. The significant mixing forms a wide, enhanced PV column. The maximum PV shifts outward. The PV redistribution therefore leads to a weak radial shear of tangential wind. The RMW is located at the radius between the two previous wind peaks. The new storm resembles an annular hurricane because of its broad tangential wind profile and a larger RMW. Since the secondary eyewall forms at a larger radius in ICE, the storm in ICE has a larger eye than that in CTL after the eyewall replacement.

5. Summary and discussion

The scientific issues associated with secondary eyewall replacement cycles include the formation of a secondary eyewall, the demise of the inner one, the organization of a new eyewall, and associated intensity fluctuation.

Sensitivity numerical experiments are carried out with the WRF model to improve our understanding of these issues. Two numerical experiments conducted in this paper utilize identical initial conditions and model parameters. The microphysics scheme (Lin et al. 1983) is modified to enhance the concentrations of freezing hydrometeors in the sensitivity experiment. An initially weak vortex spins up under idealized environmental conditions, namely a resting environment, a constant f, and a constant sea surface temperature of 29°C. Secondary eyewall replacement cycles are well simulated and the storm turns into an annular hurricane after eyewall replacement. The modified microphysics scheme enhances the concentrations of freezing hydrometeors, especially snow and ice crystals at the upper-level outflow layers. With the enhanced concentrations of ice particles, the secondary eyewall forms at a larger radius, and the storm develops into an annular hurricane with a larger eye after a slower eyewall replacement process with larger intensity fluctuation.

Diagnostic analyses are further conducted to explore the factors responsible for the different behaviors of the eyewall replacement cycles in these two experiments. Since the downdrafts are primarily maintained by cooling of snow melting, the high concentrations of snow particles in the outflow layers contribute to an enhanced moat region. The presence of the strong moat renders the secondary eyewall formation at a relatively large radial distance away from the TC center.

Axisymmetric equivalent potential temperature θ_e budget analysis is performed to understand the dissipation of the inner eyewall. A negative tendency between the concentric eyewalls associated with the downdrafts in the moat is identified. The downdrafts in the moat would import low θ_e air to the boundary layer and create a hostile condition to the inner eyewalls (Barnes et al. 1983). However, the influence of this process is relatively small and is offset by the effect of the updrafts in the model. The large negative radial advection of θ_e to the inner eyewall plays a decisive role in the demise of the inner eyewall. The boundary layer inflows with moist and warm air feed to the convection in the outer eyewall. When the outer eyewall is close to the inner eyewall, the vertically well-mixed θ_e profiles in the outer eyewall increase the radial gradient of θ_e, as well as the cold advection of entropy to the inner eyewall. The inner eyewall dissipates rapidly because of strong cold advection. Otherwise, the interception of boundary moist warm air to the inner eyewall is weak as the outer eyewall is located at a large radius.

As the inner ring weakens and eventually dies, the moat with low θ_e becomes a part of the eye. Along with the demise of the inner eyewall, the storm weakens. It reintensifies once the new eyewall recovers the ability to maintain a warm core in the original eye region and also warms up the moat region. The low θ_e airs in the moat add additional load to the new eyewall, leading to large intensity fluctuation. Therefore the storm in ICE having a clear moat tends to experience a more notable intensity fluctuation. In addition, the presence of a salient moat in ICE also yields an annular hurricane with a bigger eye after the replacement cycle.

In our study, the downdrafts in the moat do not play a major role in the collapse of the inner eyewall. It is noteworthy that their influence is possibly underestimated by the current model, since it is quite common for the numerical models to generate more convective precipitation but fewer stratiform clouds (Dai 2006). Fewer stratiform clouds can lead in turn to weaker low-level cooling and downdrafts. The deficiency of the current numerical models also possibly results in the underestimation of intensity fluctuations associated with the concentric eyewall replacement. Comparisons between the model simulation and satellite measurements in concentric eyewall cases have also been conducted and the results can be found in another paper (Zhou et al. 2011).

Concentric eyewall events can be successfully identified by utilizing passive microwave products for the global tropical cyclone monitoring network. But because of very limited spatial and temporal coverage, satellite data only provide some snapshots of TCs with concentric eyewall structures. It cannot describe the entire cycle of eyewall replacement, so it is difficult to examine the relationship between the location of secondary eyewalls and the time of eyewall replacement based on satellite images.

The results here suggest that monitoring the features of the moat region may provide a clue for the prediction of TC intensity change. This study illustrates the effect of the ice-phase particle concentration on secondary eyewall cycles, which suggests that adequate simulation of the ice phase physics is important to a successful modeling of concentric eyewall replacement cycles and the associated TC intensity changes. However, the factors that influence the concentration of ice-phase particles, especially snow, are beyond the scope of this discussion.

APPENDIX

Equations for the Equivalent Potential Temperature Budget

The WRF model equations are formulated using a terrain-following hydrostatic pressure vertical coordinate denoted by η and defined as

$$\eta = (p_h - p_{ht})/\mu, \quad (A1)$$

where $\mu = p_{hs} - p_{ht}$, p_h is the hydrostatic component of pressure, and p_{hs} and p_{ht} refer to values along the surface and top boundaries, respectively. Also,

$$\mathbf{V} = \mu\mathbf{v} = (U, V, \Omega), \quad \mathbf{v} = (u, v, \dot{\eta}), \quad \Omega = \mu\dot{\eta}, \quad (A2)$$

$$\Theta = \mu\theta, \quad \Theta_e = \mu\theta_e, \quad \text{and} \quad Q_v = \mu q_v. \quad (A3)$$

Following the method introduced by Rotunno and Emanuel (1987), the tendency equation for the equivalent potential temperature can be written as

$$\frac{\partial \Theta_e}{\partial t} = -(\nabla \cdot \mathbf{V}\theta_e) + F_{\Theta_e}, \quad (A4)$$

where $\theta_e \approx \theta + (L/C_p\pi)q_v$, and F_{Θ_e} represents a forcing term arising from subgrid-scale vertical mixing, horizontal diffusion, and dissipative heating:

$$\frac{\partial \Theta_e}{\partial t} = -(\nabla \cdot \mathbf{V}\theta) - \frac{L}{C_p\pi}(\nabla \cdot \mathbf{V}q_v) + F_\Theta + \frac{L}{C_p\pi}F_{q_v}, \quad (A5)$$

$$\frac{\partial \Theta}{\partial t} = -(\nabla \cdot \mathbf{V}\theta) + F_\Theta, \quad (A6)$$

$$\frac{\partial Q_v}{\partial t} = -(\nabla \cdot \mathbf{V}q_v) + F_{Q_v}. \quad (A7)$$

In the cylindrical coordinate

$$\frac{\partial \Theta_e}{\partial t} = -\frac{\partial V_r\theta}{\partial r} - \frac{L}{C_p\pi}\frac{\partial V_r q_v}{\partial r} - \frac{\partial V_\theta\theta}{r\partial\lambda} - \frac{L}{C_p\pi}\frac{\partial V_\theta q_v}{r\partial\lambda}$$
$$- \frac{\partial \Omega\theta}{\partial\eta} - \frac{L}{C_p\pi}\frac{\partial \Omega q_v}{\partial\eta} + F_\Theta + \frac{L}{C_p\pi}F_{q_v}. \quad (A8)$$

Separating the basic quantities into an azimuthal mean and the deviation from the azimuthal mean components and averaging the equation along the azimuthal direction, we obtain

$$\frac{\partial \overline{\Theta}_e}{\partial t} = \text{MHADV} + \text{VADV} + \text{HEDDY} + \text{DISS}, \quad (A9)$$

where

$$\text{MHADV} = -\frac{\partial \overline{V}_r\overline{\theta}}{\partial r} - \frac{L}{C_p\pi}\frac{\partial \overline{V}_r\overline{q}_v}{\partial r}, \quad (A10)$$

$$\text{VADV} = -\frac{\partial \overline{\Omega\theta}}{\partial\eta} - \frac{L}{C_p\pi}\frac{\partial \overline{\Omega q_v}}{\partial\eta}, \quad (A11)$$

$$\text{HEDDY} = -\frac{\partial \overline{V_r'\theta'}}{\partial r} - \frac{L}{C_p\pi}\frac{\partial \overline{V_r'q_v'}}{\partial r} - \frac{\partial \overline{V_\theta'\theta'}}{r\partial\lambda}$$
$$- \frac{L}{C_p\pi}\frac{\partial \overline{V_\theta'q_v'}}{r\partial\lambda}, \quad (A12)$$

$$\text{DISS} = \overline{F}_\Theta + \frac{L}{C_p\pi}\overline{F}_{q_v}. \quad (A13)$$

The four terms on the right-hand side in Eq. (9) represent contributions to the azimuthal mean θ_e budget by radial advection of azimuthal mean θ_e by azimuthal mean flow (symmetric), vertical advection, horizontal eddy, and all diabatic processes including subgrid-scale vertical mixing and horizontal diffusion and dissipative heating. To examine the contributions of downdrafts and updrafts to the azimuthal mean θ_e, the VADV term is calculated for upward and downward motion, respectively:

$$\text{VADV1} = -\frac{\partial \overline{\Omega_-\theta}}{\partial\eta} - \frac{L}{C_p\pi}\frac{\partial \overline{\Omega_-q_v}}{\partial\eta}, \quad (A14)$$

$$\text{VADV2} = -\frac{\partial \overline{\Omega_+\theta}}{\partial\eta} - \frac{L}{C_p\pi}\frac{\partial \overline{\Omega_+q_v}}{\partial\eta}. \quad (A15)$$

REFERENCES

Barnes, G. M., E. J. Zipser, D. P. Jorgensen, and F. D. Marks Jr., 1983: Mesoscale and convective structure of a hurricane rainband. *J. Atmos. Sci.,* **40,** 2125–2137.

Dai, A., 2006: Precipitation characteristics in eighteen coupled climate models. *J. Atmos. Sci.,* **19,** 4605–4630.

Emanuel, K. A., 1986: An air–sea interaction theory for tropical cyclones. Part I: Steady-state maintenance. *J. Atmos. Sci.,* **43,** 585–604.

Ge, X., T. Li, Y. Wang, and M. Peng, 2008: Tropical cyclone energy dispersion in a three-dimensional primitive equation model: Upper-tropospheric influence. *J. Atmos. Sci.,* **65,** 2272–2289.

Hawkins, J. D., M. Helveston, T. F. Lee, F. J. Turk, K. Richardson, C. Sampson, J. Kent, and R. Wade, 2006: Tropical cyclone multiple eyewall configurations. *Extended Abstracts, 27th Conf. on Hurricanes and Tropical Meteorology,* Monterey, CA, Amer. Meteor. Soc., 6B.1. [Available online at http://ams.confex.com/ams/27Hurricanes/techprogram/paper_108864.htm.]

Houze, R. A., S. S. Chen, B. F. Smull, W.-C. Lee, and M. M. Bell, 2007: Hurricane intensity and eyewall replacement. *Science,* **315,** 1235–1239.

Judt, F., and S. S. Chen, 2010: Convectively generated potential vorticity in rainbands and formation of the secondary eyewall in Hurricane Rita of 2005. *J. Atmos. Sci.,* **67,** 3581–3599.

Kain, J. S., and J. M. Fritsch, 1990: A one-dimensional entraining/detraining plume model and its application in convective parameterization. *J. Atmos. Sci.,* **47,** 2784–2802.

——, and ——, 1993: Convective parameterization for mesoscale models: The Kain–Fritsch scheme. *The Representation of Cumulus Convection in Numerical Models, Meteor. Monogr.,* No. 46, Amer. Meteor. Soc., 165–170.

Knaff, J. A., J. P. Kossin, and M. DeMaria, 2003: Annular hurricanes. *Wea. Forecasting,* **18,** 204–223.

——, T. A. Cram, A. B. Schumacher, J. P. Kossin, and M. DeMaria, 2008: Objective identification of annular hurricanes. *Wea. Forecasting,* **23,** 17–28.

Kossin, J. P., and M. Sitkowski, 2009: An objective model for identifying secondary eyewall formation in hurricanes. *Mon. Wea. Rev.,* **137,** 876–892.

——, W. H. Schubert, and M. T. Montgomery, 2000: Unstable interactions between a hurricane's primary eyewall and a secondary ring of enhanced vorticity. *J. Atmos. Sci.,* **57,** 3893–3917.

Kuo, H.-C., L.-Y. Lin, C.-P. Chang, and R. T. Williams, 2004: The formation of concentric vorticity structures in typhoons. *J. Atmos. Sci.,* **61,** 2722–2734.

——, W. H. Schubert, C.-L. Tsai, and Y.-F. Kuo, 2008: Vortex interactions and barotropic aspects of concentric eyewall formation. *Mon. Wea. Rev.,* **136,** 5183–5198.

——, C.-P. Chang, Y.-T. Yang, and H.-J. Jiang, 2009: Western North Pacific typhoons with concentric eyewalls. *Mon. Wea. Rev.,* **137,** 3758–3770.

Lin, Y.-L., R. D. Farley, and H. D. Orville, 1983: Bulk parameterization of the snow field in a cloud model. *J. Climate Appl. Meteor.,* **22,** 1065–1092.

Liu, Y., A. Bourgeois, T. Warner, S. Swerdlin, and J. Hacker, 2005: Implementation of observation-nudging based FDDA into WRF for supporting ATEC test operations. *Proc. 2005 WRF User Workshop,* Boulder, CO, NCAR, 10.7. [Available online at http://www.rap.ucar.edu/projects/armyrange/references/publications/Liu_WRF-WK.2005.pdf.]

Lord, S. J., H. E. Willoughby, and J. M. Piotrowicz, 1984: Role of a parameterized ice-phase microphysics in an axisymmetric tropical cyclone model. *J. Atmos. Sci.,* **41,** 2836–2848.

Molinari, J., and D. Vollaro, 1990: External influences on hurricane intensity. Part II: Vertical structure and response of the hurricane vortex. *J. Atmos. Sci.,* **47,** 1902–1918.

Montgomery, M. T., and R. J. Kallenbach, 1997: A theory for vortex Rossby waves and its application to spiral bands and intensity changes in hurricanes. *Quart. J. Roy. Meteor. Soc.,* **123,** 435–465.

Noh, Y., W. G. Cheon, S. Y. Hong, and S. Raasch, 2003: Improvement of the K-profile model for the planetary boundary layer based on large eddy simulation data. *Bound.-Layer Meteor.,* **107,** 401–427.

Nong, S., and K. Emanuel, 2003: A numerical study of the genesis of concentric eyewalls in hurricanes. *Quart. J. Roy. Meteor. Soc.,* **129,** 3323–3338.

Rotunno, R., and K. A. Emanuel, 1987: An air–sea interaction theory for tropical cyclones. Part II: Evolutionary study using a nonhydrostatic axisymmetric numerical model. *J. Atmos. Sci.,* **44,** 542–561.

Rozoff, C. M., W. H. Schubert, B. D. McNoldy, and J. P. Kossin, 2006: Rapid filamentation zones in intense tropical cyclones. *J. Atmos. Sci.,* **63,** 325–340.

——, ——, and J. P. Kossin, 2008: Some dynamical aspects of tropical cyclone concentric eyewalls. *Quart. J. Roy. Meteor. Soc.,* **134,** 583–593.

Samsury, C. E., and E. J. Zipser, 1995: Secondary wind maxima in hurricanes: Airflow and relationship to rainbands. *Mon. Wea. Rev.,* **123,** 3502–3517.

Shapiro, L. J., and H. E. Willoughby, 1982: The response of balanced hurricanes to local sources of heat and momentum. *J. Atmos. Sci.,* **39,** 378–394.

Terwey, W. D., and M. T. Montgomery, 2008: Secondary eyewall formation in two idealized, full-physics modeled hurricanes. *J. Geophys. Res.,* **113,** D12112, doi:10.1029/2007JD008897.

Willoughby, H. E., 1995: Mature structure and evolution: Tropical cyclone structure and structure change. WMO Rep. TCP-38, 21–62.

——, J. A. Clos, and M. G. Shoreibah, 1982: Concentric eyewalls, secondary wind maxima, and the evolution of the hurricane vortex. *J. Atmos. Sci.,* **39,** 395–411.

——, H.-L. Jin, S. J. Lord, and J. M. Piotrowicz, 1984: Hurricane structure and evolution as simulated by an axisymmetric, nonhydrostatic numerical model. *J. Atmos. Sci.,* **41,** 1169–1186.

Zhou, X., and B. Wang, 2009: From concentric eyewall to annular hurricane: A numerical study with the cloud-resolved WRF model. *Geophys. Res. Lett.,* **36,** L03802, doi:10.1029/2008GL036854.

——, ——, X. Ge, and T. Li, 2011: Impact of secondary eyewall heating on tropical cyclone intensity change. *J. Atmos. Sci.,* **68,** 450–456.